

1

2 **Submesoscales are a significant turbulence source in global** 3 **ocean surface boundary layer**

4

5 Jihai Dong^{1,2*}, Baylor Fox-Kemper³, Jacob O. Wenegrat⁴, Abigail S. Bodner⁵, Xiaolong Yu⁶,
6 Stephen Belcher⁷, Changming Dong^{1,2*}

7 ¹School of Marine Sciences, Nanjing University of Information Science and Technology, Nanjing,
8 China

9 ²Southern Marine Science and Engineering Guangdong Laboratory (Zhuhai), Zhuhai, China,

10 ³Department of Earth, Environmental, and Planetary Sciences, Brown University, Providence,
11 Rhode Island, USA

12 ⁴Department of Atmospheric and Oceanic Science, University of Maryland, College Park, College
13 Park, Maryland, USA

14 ⁵Earth, Atmospheric, and Planetary Sciences, Massachusetts Institute of Technology,
15 Cambridge, MA, USA

16 ⁶School of Marine Sciences, Sun Yat-sen University, Zhuhai, China

17 ⁷Met Office Hadley Centre, Exeter, UK

18

19 *Corresponding authors: Changming Dong, cmdong@nuist.edu.cn; Jihai Dong,
20 jihai_dong@nuist.edu.cn

21

22 **Keywords:** ocean surface boundary layer; turbulent mixing; Langmuir turbulence; front;
23 submesoscale

24

25

26 **Abstract**

27 The turbulent ocean surface boundary layer is a key part of the climate system affecting both the
28 energy and carbon cycles. Accurately simulating the boundary layer is critical in improving climate
29 model performance, which deeply relies on our understanding of the turbulence in the boundary
30 layer. Turbulent energy sources in the boundary layer are traditionally believed to be dominated
31 by waves, winds and convection. Recently, submesoscale phenomena with spatial scales of
32 0.1~10 km at ocean fronts have been shown to also make a contribution. Here, by applying a
33 non-dimensional turbulent kinetic energy budget equation, we show that the submesoscale
34 geostrophic shear production at fronts is a significant turbulent energy source within the ocean
35 boundary layer away from the sea surface. The contribution reaches 34% of the total dissipation
36 in winter and 17% in summer at the mid-depth of the boundary layer, despite its intermittency in
37 space and time. This work indicates fundamental deficiencies in previous conceptions of ocean
38 boundary layer turbulence, and invites a reappraisal of the sampling scale in observations, model
39 resolution and parameterizations, and other consequences of the global energy budget.

40
41 **Introduction**

42
43 The ocean surface boundary layer (OSBL), a turbulent upper layer in the ocean, provides the
44 channel for the atmosphere to communicate with the ocean interior. Intense air-sea exchanges of
45 momentum and heat energize small-scale (<100 m) turbulence and make the OSBL the most
46 turbulent layer in the ocean¹. OSBL turbulence modulates the transfer of momentum, heat and
47 dissolved gases between the sea surface and ocean interior. These exchanges affect the water
48 properties of the ocean, thereby influencing climate variability on timescales from days to
49 centuries^{2,3,4,5,6}. Turbulence also enhances the upward flow of nutrients to the light-filled
50 biologically-productive layers, a control on primary ocean productivity^{7,8}. OSBL turbulence is not
51 resolved in most ocean and climate models and is usually represented by parameterizations.

52
53 Studies in the last decades have been conducted to quantify the contributions from OSBL
54 processes including winds, waves, and convection^{9,10,11} to OSBL turbulence. These prior
55 assessments focused only on the sources of turbulent kinetic energy (TKE) that are effectively
56 one-dimensional—consistent with classical conceptions of boundary layer turbulence and easily
57 determined by the available data and models. Extensive work has now documented that OSBL
58 turbulence can be significantly altered in frontal regions with strong vertical shears providing a
59 significant source of TKE via submesoscale phenomena with spatial scales of 0.1~10km¹².
60 Observations also show that classical scalings of OSBL turbulence are deficient^{13,14}, while a
61 significant contribution of fronts to OSBL turbulence has been reported^{15,16,17}. This geostrophic
62 shear production turbulence (GSP) source due to submesoscales relies on horizontal buoyancy
63 gradients and is therefore fundamentally informed by two-dimensional flow parameters. This
64 mixing is important for both vertical and horizontal exchange of properties at ocean fronts, but is
65 not included in prior global assessments of OSBL turbulence, nor currently widely-used
66 parameterizations^{18,19}.

67
68 In this work, GSP is found to be a significant, yet highly intermittent, contributor to global OSBL
69 turbulence away from the sea surface. To show this we extend the Belcher et al.¹⁰ approach to
70 determining sources of TKE production by surface forcing to include GSP contributions, and we
71 compare the relative significance of four kinds of turbulence: geostrophic shear production
72 turbulence at fronts (GSP), Langmuir shear production turbulence due to waves (LSP),
73 ageostrophic shear production turbulence due to surface wind stress (AGSP) and vertical
74 buoyancy production turbulence due to surface buoyancy loss (VBP) in the global OSBL. **GSP is
75 found to be a leading contributor to turbulence at the mid-depth of the OSBL in winter.** The result
76 is robust to the analysis choices, and provides a clue to reasons for the OSBL bias in ocean and
77 climate model simulations and a direction to improve model capability for climate change
78 projections.

79

80 **Results**

81

82 **Distributions of the turbulence sources**

83 The relative contributions of four sources of turbulence, waves (LSP), fronts (GSP), surface
 84 buoyancy loss (VBP) and wind (AGSP) to OSBL turbulence are determined by three non-
 85 dimensional parameters, the turbulent Langmuir number La_t , the ratio of the boundary layer
 86 depth to the Langmuir stability length h/L_L , and the ratio of the boundary layer depth to the
 87 geostrophic shear stability length h/L_s (**Methods**). The relative importance of wind forcing, waves,
 88 buoyancy convection and geostrophic shear are reflected by location along the three axes of the
 89 plots in **Fig. 1**.

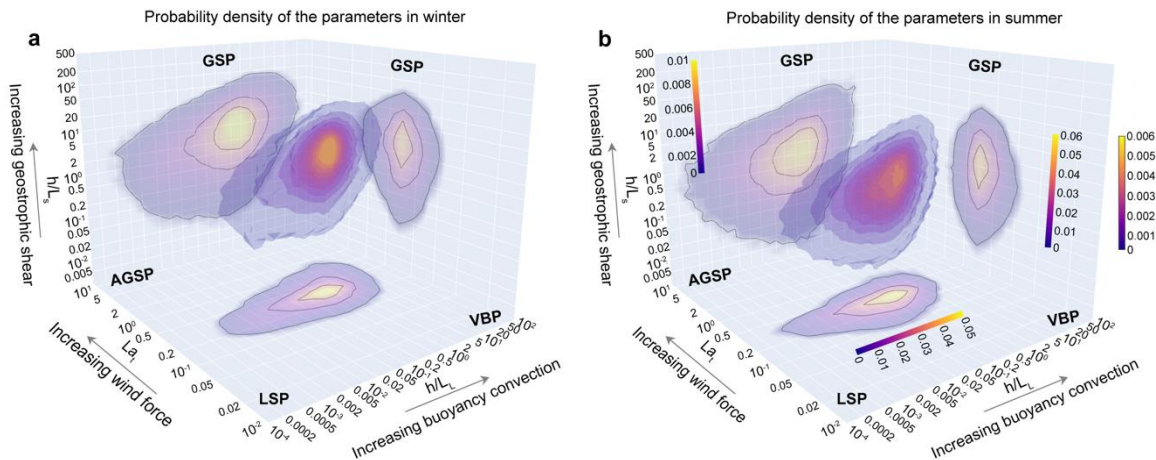
90

91 La_t of the x-axis governs the wind-forced turbulence source (AGSP) against the wave-forced
 92 turbulence source (LSP), and LSP dominates over AGSP when $La_t < 0.3$ ¹⁰. The global
 93 distribution of La_t shows seasonality of LSP and AGSP consistent with that found in Belcher et al.
 94¹⁰. The parameter h/L_L of the y-axis measures the source of convective turbulence (VBP) against
 95 LSP. Large h/L_L values ($h/L_L > 1$) indicate a dominant role of VBP over LSP. This ratio is much
 96 larger in winter (generally > 1), implying a generally more dominant role of LSP over VBP.
 97

98

99 To measure the relative GSP magnitude, the ratio h/L_s is used²⁰. The geostrophic shear stability
 100 length L_s depends on the strength of horizontal buoyancy gradients associated with fronts.
 101 Estimation of this quantity requires a rescaling of the resolved model buoyancy gradients, which
 102 is done assuming frontal arrest under the Turbulent Thermal Wind balance (TTW; **Methods**)²¹,
 103 although we emphasize that major results are qualitatively robust to this choice as assessed
 104 below. Much of the estimated global distribution is characterized by $h/L_s > 1$ in the z-axis,
 105 indicating the frontal contribution to TKE production (GSP) dominates over wind-forced
 106 turbulence (AGSP). Seasonal variation of h/L_s is also significant, with larger h/L_s values in winter
 107 resulting from more active submesoscale fronts with intense horizontal density gradients²² that
 108 outpace the enhanced AGSP associated with winter storms.

109



110

111 **Fig. 1 Three-dimensional global probability density of the three parameters. a,** The
 112 probability density in winter. **b,** The probability density in summer. The three parameters are
 113 turbulent Langmuir number La_t of the x-axis, the ratio of the boundary layer depth to the Langmuir
 114 stability length h/L_L of the y-axis, and the ratio of the boundary layer depth to the geostrophic
 115 shear stability length h/L_s of the z-axis. Two-dimensional projections of the distributions are also
 116 shown. The black contours enclose 30%, 60%, and 90% of the global values. Each source of
 117 turbulence is labeled (GSP: geostrophic shear production turbulence; LSP: Langmuir shear
 production turbulence; VBP: vertical buoyancy production turbulence; AGSP: ageostrophic shear

118 production turbulence) and the contribution of fronts (i.e., GSP) is highlighted as the geostrophic
119 shear along the z-axis is increased. Source data are provided as a Source Data file.

120

121 **Dissipation regimes in parameter space**

122 Two-dimensional probability distribution slices overlapped on regime maps derived from **Fig. 1**
123 are shown (**Fig. 2**). The La_t - h/L_L projection, neglecting the geostrophic shear, has been discussed
124 by Belcher et al. and Li et al.^{10,11} who argued for a significant role of LSP in generating OSBL
125 turbulence. As the parameter h/L_s is introduced, the regimes are changed. The percentiles
126 indicate that the global OSBL is generally under LSP and LSP/VBP regimes for locations with
127 weak geostrophic shears (**Fig. 2a**). GSP begins to play a role while LSP and AGSP are
128 weakened as the geostrophic shear increases (**Fig. 2d,g**).

129

130 The La_t - h/L_s space shows the dependence of the regimes on buoyancy convection. When the
131 surface buoyancy convection is weak, the enclosed contours show that most of the locations are
132 dominated by LSP, GSP and their mixed regime, indicating an important role of GSP globally in
133 these conditions (**Fig. 2b**). The contribution of LSP turbulence is finally eliminated as the surface
134 buoyancy loss continues to increase, and GSP and VBP dominate OSBL turbulence (**Fig. 2e,h**).

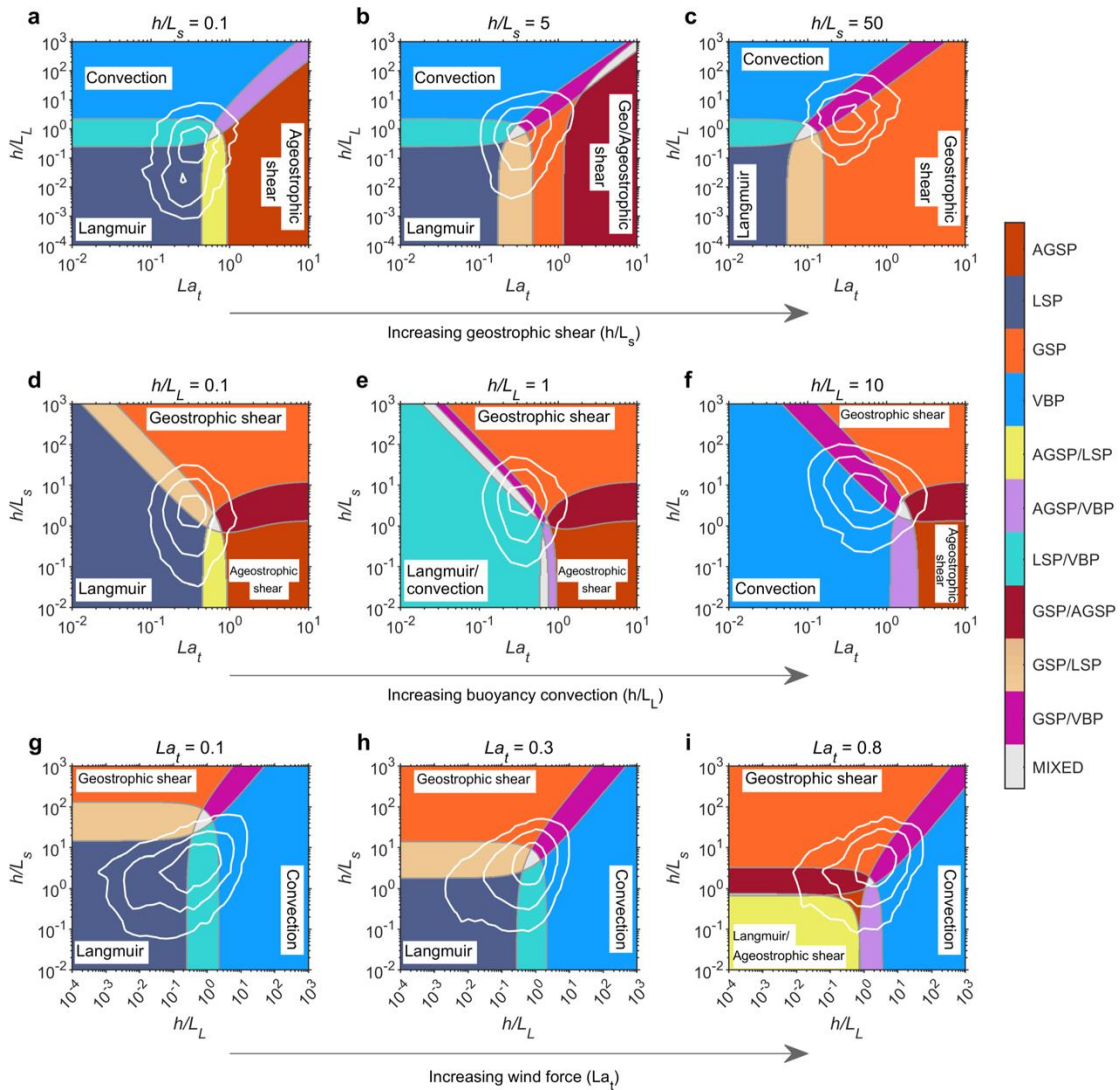
135

136 In the h/L_L - h/L_s space, LSP and VBP dominate OSBL turbulence when La_t is small (**Fig. 2c**). The
137 percentile distributions show that almost 90% of the locations with small La_t are dominated by
138 LSP, VBP and their mixed regimes. As the wind forcing becomes stronger, the contribution from
139 LSP is decreased but GSP and AGSP become more important. When the wind forcing is
140 sufficiently strong, more than 90% of the corresponding locations are under a mix of AGSP, GSP,
141 VBP (**Fig. 2i**).

142

143 In summer, as the wind force, buoyancy loss and geostrophic shear are all weakened, the
144 distributions of these parameters are shifted to small values (**Supplementary Fig. 1**). The role of
145 LSP is generally strengthened, while other turbulence sources are weakened. In particular, the
146 relative importance of GSP is weakened from winter to summer, which is the opposite behavior of
147 LSP.

148



149
150
151
152
153
154
155
156
157
158
159
160
161
162
163

Fig. 2 Turbulence regimes in parameter slices in winter. **a**, $h/L_s=0.1$. **b**, $h/L_s=5$. **c**, $h/L_s=50$. **d**, $h/L_L=0.1$. **e**, $h/L_L=1$. **f**, $h/L_L=10$. **g**, $La_t=0.1$. **h**, $La_t=0.3$. **i**, $La_t=0.8$. The regimes (GSP: geostrophic shear production turbulence; LSP: Langmuir shear production turbulence; VBP: vertical buoyancy production turbulence; AGSP: ageostrophic shear production turbulence) denoted by different color patches are defined by the dominant production terms in the turbulent kinetic energy (TKE) budget. The white contours enclose 30%, 60%, and 90% of the locations with the corresponding values. A regime is considered dominant when its contribution exceeds 75% of the total dissipation, otherwise, it is a two-turbulence-mixed regime when two TKE sources both contribute more than 25% while all others contribute less than 25%, and lastly, it is a mixed regime if more than three sources of turbulence contribute more than 25% ¹¹. The distributions indicate that GSP is an important regime for ocean surface boundary layer turbulence over the globe, especially at locations with strong frontal geostrophic shears. Source data are provided as a Source Data file.

Dissipation magnitudes globally

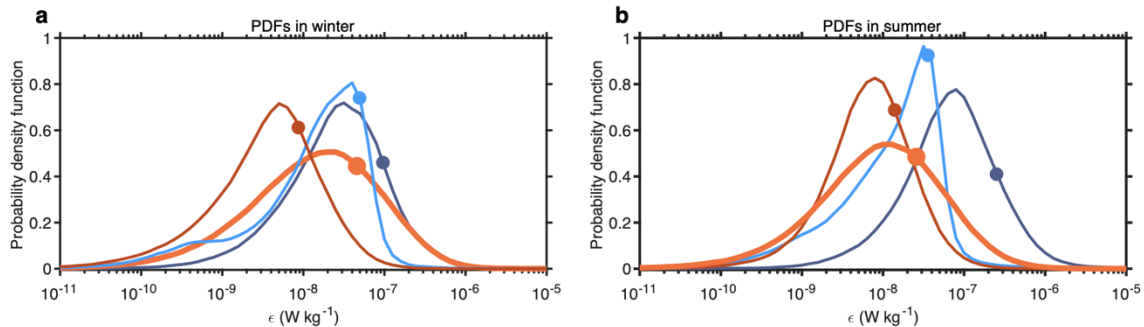
164
165
166
167

According to both mean and median absolute dissipation rates, LSP has the largest magnitude in both seasons (**Fig. 3; Supplementary Fig. 2**). The dominant role of LSP has been reported by previous studies ^{10,11}. Without considering GSP, Li et al. ¹¹ found the OSBL is dominated by LSP

168 (e.g., the Southern Ocean), or VBP (e.g., tropical regions), and mixed LSP and VBP (i.e., mid-
 169 latitude regions). By contrast, GSP is here shown to often be larger than the VBP and AGSP
 170 contributions, and to rival LSP in winter. GSP is stronger in winter, especially so in the western
 171 boundary currents and the Southern Ocean. Overall, the relative contributions of GSP to the total
 172 dissipation averaged over the globe are 35% in winter and 18% in summer.

173
 174
 175
 176
 177
 178
 179
 180
 181
 182
 183

Probability density functions (PDFs) of all turbulence sources show nearly log-skew-normal
 distributions (**Fig. 3**), consistent with both intermittent alternating energy sources²³ and the
 forward cascade of oceanic turbulence²⁴. In such distributions, the large mean rates are
 determined by intermittent extreme events, rather than the accumulation. Compared with the
 other sources, GSP has the widest distribution, implying it has the highest intermittency and the
 greatest difference between its average and median values. This highlights a challenge in
 observational estimates of integrated contributions of frontal turbulence. Extremely sharp fronts,
 while covering very limited spatial extent and oftentimes being transient, can be associated with
 sufficiently large GSP so as to significantly influence the mean values.



184
 185
 186
 187
 188
 189
 190
 191
 192
 193
 194
 195
 196

Fig. 3 Probability density functions (PDFs) of the turbulence sources. **a**, PDFs of the four sources, geostrophic shear production turbulence (GSP; orange), Langmuir shear production turbulence (LSP; dark blue), vertical buoyancy production turbulence (VBP; light blue), ageostrophic shear production turbulence (AGSP; dark red). in winter. **b**, PDFs of the four sources in summer. The dots indicate the corresponding global mean value of each distribution. The log-normal distribution of the PDFs suggests that the mean and integral of ocean surface boundary layer dissipation are determined by intermittent high dissipation rates. The highest intermittency of GSP can also be derived from the distributions. Source data are provided as a Source Data file.

197
 198
 199
 200
 201
 202
 203
 204
 205
 206
 207
 208

Turbulent energy sources globally

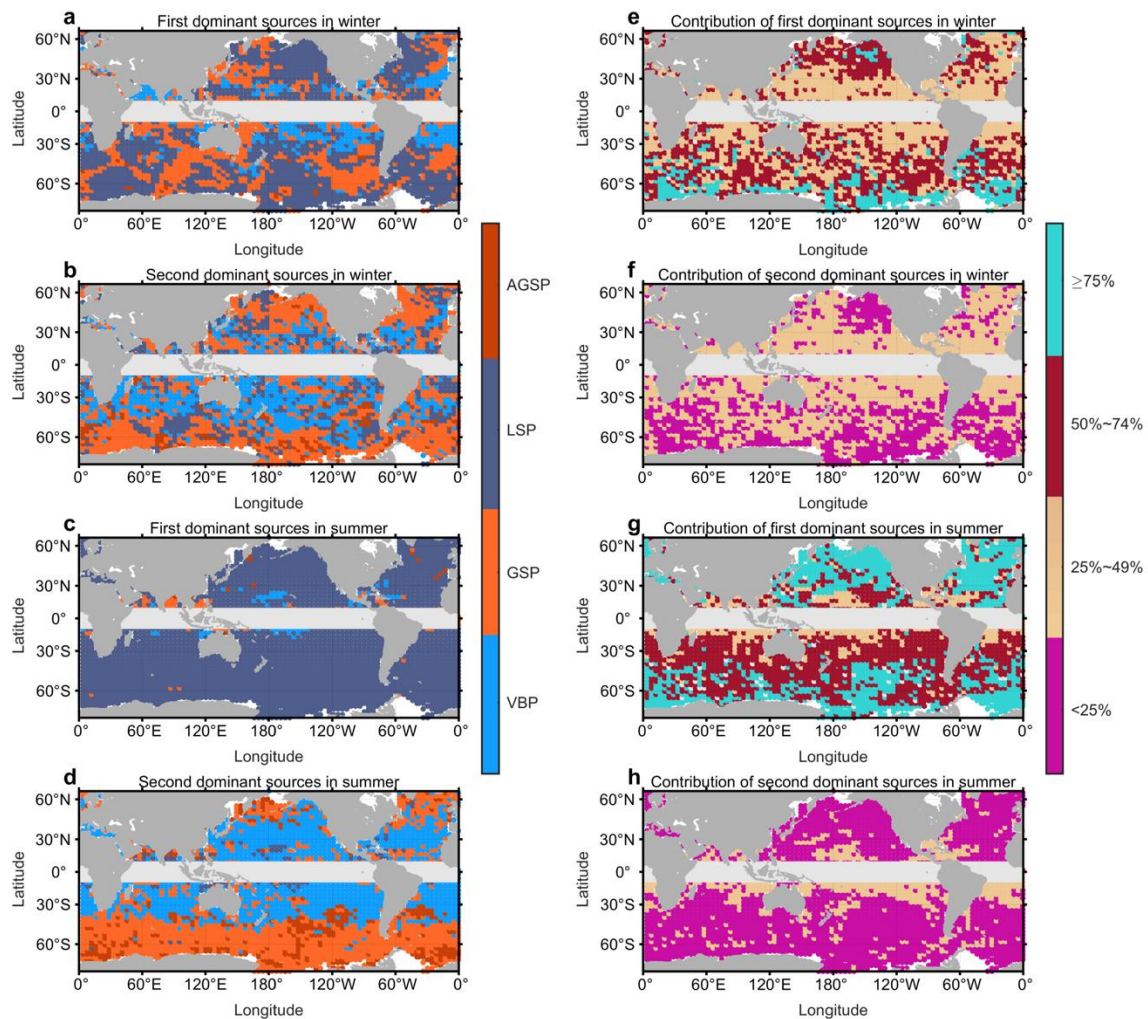
The spatial distribution of the global turbulence sources can be determined by ranking the relative contributions of the four sources by location. **Fig. 4** maps the top two turbulence sources over the globe and the associated contributions relative to the total dissipation in different seasons. In winter, LSP is the most spatially prevalent source, accounting for 44% of the global locations, especially at mid and high latitudes (**Fig. 4a**). The spatial prevalence of GSP is 37% and is most common at low and mid latitudes, while some locations at low latitudes are controlled by VBP (16% of all locations). A latitudinal dependence in the percentage contribution of the principal source is evident, with the largest source generally contributing less than 50% of the total dissipation at low latitudes, growing to larger than 75% at high latitudes. The contribution of VBP (35%) and GSP (34%) become the most dominant regimes in the map of the secondary sources (**Fig. 4b**).

209
 210
 211

Overall, considering the top two sources, GSP is the most spatially extensive primary source, providing a leading contribution to turbulence in 71% of the locations considered. By contrast, it is 70% for LSP and 51% for VBP. Moreover, the relative contribution of GSP explicitly shows where

212 GSP dominates OSBL turbulence, such as the western North Pacific Ocean, the Eastern North
 213 Atlantic Ocean in winter, and the Southern Ocean in both seasons (**Supplementary Fig. 3**).
 214 Thus, while individual sharp fronts cover very limited spatial area, their contribution to OSBL
 215 turbulence may have broad impact.

216
 217 In summer the distribution of energy sources changes, consistent with changes in surface forcing
 218 and the known seasonality of submesoscale turbulence^{22, 25, 26}. LSP is the most spatially-
 219 prevalent source over the globe, except for a few tropical regions with significant GSP and VBP
 220 contributions. LSP accounts for 84% of all summer locations, much larger than other sources
 221 (11% for GSP and 4% for VBP). This dominance is highlighted by the relative contribution shown
 222 in **Fig. 4g**, which indicates that the LSP may be responsible for more than 50% of global OSBL
 223 turbulence production outside of the tropics. For the second dominant sources, it is GSP at high
 224 latitudes while VBP at low latitudes (**Fig. 4d**).
 225



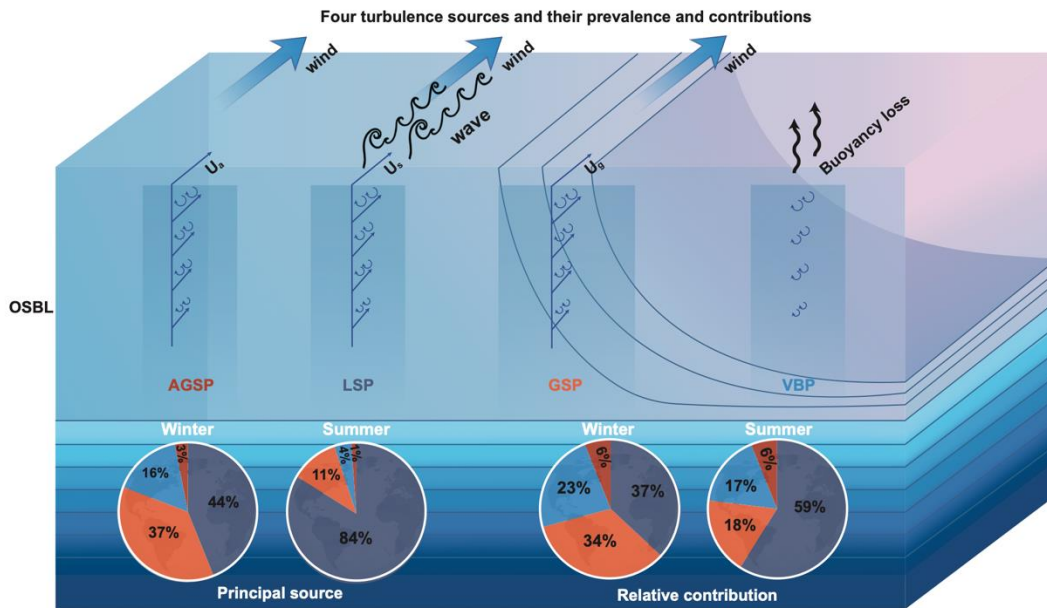
226
 227 **Fig. 4 Global distributions of the two most likely dominant sources at each location. a,** The
 228 first most likely dominant sources (GSP: geostrophic shear production turbulence; LSP: Langmuir
 229 shear production turbulence; VBP: vertical buoyancy production turbulence; AGSP: ageostrophic
 230 shear production turbulence) in winter. **b,** The second most likely dominant sources in winter. **c,**
 231 The first most likely dominant sources in summer. **d,** The second most likely dominant sources in
 232 summer. Their relative contribution percentages to the total mean dissipation (%) are shown in **e-**

233 h. The relative contributions shown in e-h indicate that the summation of the top two sources can
 234 explain most ($Pct_{1st} + Pct_{2nd} > 55\%$) of the total dissipation. GSP turbulence is the first largest
 235 contributor at low and mid latitudes in winter, and still the second largest contributor at high
 236 latitudes in both seasons. Source data are provided as a Source Data file.

237

238 **Discussion**

239 The results here suggest that ocean fronts make a leading-order contribution to OSBL turbulence
 240 in many parts of the global ocean. This result differs fundamentally from classic conceptual
 241 models assuming horizontally uniform flows, and it implies parameterizations of OSBL turbulence
 242 that account only for wind, wave, and convective sources of turbulence are deficient. A schematic
 243 diagram of the four kinds of turbulence sources and their relative contributions is shown in Fig. 5.
 244 Nevertheless, its quantitative estimation heavily relies on the robustness of the calculation of the
 245 horizontal buoyancy gradient. Here the robustness of these results is also tested by using other
 246 two alternative methods.



247

248 **Fig. 5 A schematic diagram of the four turbulence sources.** Geostrophic shear production
 249 turbulence (GSP), Langmuir shear production turbulence (LSP), vertical buoyancy production
 250 turbulence (VBP), and ageostrophic shear production turbulence (AGSP) represent the
 251 turbulence sources from Langmuir circulation, geostrophic current shear, vertical convection, and
 252 ageostrophic current shear. LSP is the shear to turbulence from Stokes drifts due to winds and
 253 waves. GSP is the shear to turbulence from geostrophic currents at fronts with down-front winds.
 254 VBP is the convection to turbulence by gravitational instability due to surface buoyancy loss.
 255 AGSP is the shear to turbulence from ageostrophic currents induced by winds. The left two pie
 256 charts show the spatial prevalence of each turbulence source in winter and summer, while the
 257 right two show the relative contribution of each source to the total dissipation magnitude averaged
 258 over the globe (LSP: dark blue; GSP: orange; VBP: light blue; AGSP: dark red). These
 259 percentages indicate that GSP is a prevalent and significant source of OSBL turbulence over the
 260 globe. Source data are provided as a Source Data file.

261

262

263 First, GSP is calculated based directly on the raw resolved buoyancy gradients of the numerical
 264 model (“uncorrected” method). These estimates can therefore be thought of as a conservative
 265 lower bound^{21,27}. Second, we rescale the buoyancy gradients by assuming a horizontal
 266 buoyancy density gradient spectrum consistent with white noise from the effective resolution

267 down to the frontal arrest scale (“no-slope” method)²⁸. This approach leads to a larger estimate
268 of the horizontal buoyancy gradient (or smaller L_s), and thus provides an upper bound of GSP
269 dissipation.

270
271 Unsurprisingly, the role of GSP is weakened for the uncorrected case, while it is strengthened for
272 the no-slope case (**Supplementary Fig. 4 and S5**). Taking the uncorrected and no-slope
273 estimates as effective upper and lower uncertainty bounds, the mean relative contributions of
274 GSP are 34% with the uncertainty of [27%, 37%] in winter and 17% [16%, 18%] in summer. The
275 dominant locations for each energy source and their averages and percentiles (**Supplementary**
276 **Table 1**) indicate that GSP still emerges as a major global source of TKE in the boundary layer
277 even when using the most conservative approach of estimating the horizontal buoyancy gradient
278 directly from the marginally submesoscale-permitting 1/48° model run solution, suggesting the
279 robust role of fronts in energizing global boundary layer turbulence.

280 The turbulence sources discovered here are only applicable under down-front wind component
281 and destabilizing conditions. According to our evaluation, the conditions are met about 31% and
282 21% of the time in winter and summer (the globally-averaged percentages of times with down-
283 front wind component and destabilizing conditions over the whole months), respectively. It
284 means GSP contributes 34% in a third of the winter. This is the most conservative estimation
285 since even in up-front wind conditions GSP is expected to have a vertical structure similar to
286 AGSP^{20,29} and a comparable magnitude of the GSP contribution to the down-front case will be
287 derived. If we assume the parameter $A_G=0.5$ in the TKE equation (see Methods) is still applicable
288 in up-front conditions, the GSP contribution will become 35% [28%, 38%] in 65% of winter and
289 18% [17%, 19%] in 40% of summer. Meanwhile, the TKE model is a linear superposition of
290 different kinds of turbulence and their interactions are not considered. For strong baroclinic fronts,
291 VBP turbulence is inhibited and the surface buoyancy flux tends to characterize GSP turbulence
292¹⁸. Likewise, frontal processes, such as mixed layer instability, tend to restratify the OSBL and
293 generate positive VBP, also reducing the VBP dominance^{30,31}. The full range of these types of
294 interactions between turbulence energy sources is not yet known, however additional work on this
295 topic will help further refine future estimates of the global sources of OSBL turbulence.

296
297 It is noteworthy that the relative contributions of the turbulence sources vary with depth within the
298 OSBL, as the vertical decreasing rates of their intensities are different. The relative contribution at
299 the OSBL mid-depth revealed in this work suggests a significant role of GSP turbulence to the
300 exchanges between the OSBL and the ocean interior. However, its contribution is not
301 represented in most regional and climate ocean models, which may be hypothesized to be one of
302 the key reasons leading to simulated biases of the OSBL. Due to the small frontal arrest scale,
303 parameterizing GSP turbulence, as would be natural in a model with strict kinetic energy
304 conservation³², offers an alternative future approach to include its contribution in ocean models.
305 Despite that a scheme parameterizing GSP has been proposed¹⁸, limitations should be noted
306 (such as the rescaling of the frontal buoyancy gradient is not considered) and further research is
307 needed.

308

309 **Methods**

310

311 **Model data**

312 Oceanic data including velocity, temperature, and salinity are from a submesoscale-permitting
313 global model, LLC4320. LLC4320 was simulated by the Massachusetts Institute of Technology
314 general circulation model (MITgcm) on a Latitude-Longitude polar Cap (LLC) grid^{33,34}. The model
315 has a spatial resolution of 1/48° and 90 vertical layers. The model was initialized successively
316 from a set of simulations with resolutions of 1/6°, 1/12°, and 1/24°. The K-Profile Parameterization
317 scheme (KPP) was applied in the simulation. The atmospheric forcing to drive the simulation was
318 from the European Centre for Medium Range Weather Forecasting (ECMWF) with resolutions of
319 6 hours in time and 0.14° in space. Tidal forcing was also included in the simulation. LLC4320
320 was run for 14 months of simulation time, from September 2011 to November 2012, and essential

321 state variables were stored at hourly snapshots. The model result has been validated against in
322 situ observations^{34, 35} and has been widely used for the analysis of submesoscale seasonality,
323 energy cascade and air-sea flux^{22, 25, 36}. The ECMWF surface fluxes are applied to evaluate
324 OSBL turbulence. For consistency, we directly use the outputted sea surface fluxes from the
325 simulation, except for the Stokes drift—from ECMWF ERA5 which has a spatial resolution of 0.5°.
326 In this work, data in February and August are chosen for analysis. All results shown in this work
327 are subsampled with a grid spacing of 4°.

328
329 Before the LLC4320 data are used for further analysis, the performance of LLC4320 in
330 reproducing OSBL fronts needs to be assessed. However, a direct assessment of the buoyancy
331 gradients is impossible since high resolution global observations are not available. Considering
332 satellite-derived sea surface temperature (SST) usually have high spatial resolution around 1 km,
333 a quantitative comparison of SST between LLC4320 and Visible Infrared Imaging Radiometer
334 Suite (VIIRS) L2 products (with spatial resolutions from 0.75 km at nadir to 1.5 km at the swath
335 edge) is conducted. Here, SST from LLC4320 is the uppermost 0.5-m layer of the simulation.
336 Recently, LLC4320 is demonstrated to reproduce the observed distribution of SST patterns well
337 both globally and regionally³⁷. Nevertheless, as OSBL fronts are focused in this work, the spatial
338 SST variance is assessed using the first-order structure function³⁸. As the VIIRS L2 data have
339 missing values due to clouds, the structure function can avoid the effect of these missing values
340 and statistically demonstrates the capability of the LLC4320 model in reproducing SST variances.

341
342 The first-order structure function here is defined as the difference of SST between the pair of
343 points, \mathbf{x} , and $\mathbf{x} + \mathbf{r}$, namely,

$$\delta = SST(\mathbf{x} + \mathbf{r}) - SST(\mathbf{x}) \quad (1)$$

344
345 Then the probability density functions (PDFs) of SST structure function δ at different scales ($r =$
346 100 km, 80 km, 60 km, 50km, 40 km, 30 km, 20 km, 10km and 5 km) are calculated based on
347 VIIRS and LLC4320 data in the same period (February and August of 2012). To avoid the effect
348 of the missing values in VIIRS, we interpolate the LLC4320 data onto the VIIRS grids at the
349 corresponding dates, and then avoid the corresponding missing-value regions. Due to the spatial
350 resolution limitation, the structure function probabilities of large separations r from LLC4320 are
351 expected to be consistent with VIIRS. But as r decreases below the effective resolution, the PDFs
352 from LLC4320 are speculated to underestimate the SST frontal magnitude from VIIRS. The
353 calculated PDF differences between these two datasets in different regions confirm the
354 speculation (**Supplementary Fig. 6**). The negligible differences between LLC4320 and VIIRS on
355 separation scales larger than the effective resolution indicate that LLC4320 reproduces observed
356 SST jumps well. However, as the scale decreases below the effective resolution, the
357 underprediction of SST jumps begins to become more and more consequential. The positive bias
358 in probability at small SST jump magnitude and negative bias in probability at large SST jump
359 magnitude imply that at small spatial scale LLC4320 overpredicts small SST jumps and
360 underpredicts large SST jumps compared to the real ocean. So, this misestimation is corrected
361 on the buoyancy gradients (see the method below).

362
363 In addition to SST, we further evaluate the capability of the LLC4320 simulation to reproduce the
364 OSBL thickness which is a crucial factor in determining the dissipation magnitudes. However, a
365 direct comparison of the OSBL thickness to observation is currently impossible. Here, we
366 compare it to the surface mixed layer from LLC4320 and Argo observations (**Supplementary Fig.**
367 **7**), since they should be dynamically close after temporally averaging. The temporally averaged
368 OSBL thickness is close to the mixed layer thickness in LLC4320 (the root mean squares of the
369 bias are less than 5 m over the globe) which tends to simulate relatively deeper mixed layer
370 depths compared to the observations, especially in the winter month (the root mean square of the
371 global mixed layer thickness bias is 13.5 m in February but 24.4 m in August). This may be
372 attributed to the unresolved restratifying processes such as small-scale mixed layer instability and
373 symmetric instability^{27, 39}. Nevertheless, compared to the observations, despite the quantitative

374 bias, the global pattern of the layer thicknesses from LLC4320 generally resembles the observed
 375 one in different seasons.

376
 377 **Non-dimensional turbulent kinetic energy budget**

378 The TKE budget in the OSBL can be expressed as follows:

379
$$\frac{\partial e}{\partial t} = -\overline{\mathbf{u}'w'} \frac{\partial \overline{u_s}}{\partial z} - \overline{\mathbf{u}'w'} \frac{\partial \overline{u_g}}{\partial z} - \overline{\mathbf{u}'w'} \frac{\partial \overline{u_a}}{\partial z} + \overline{w'b'} - \epsilon + F_e. \quad (2)$$

380 Here, the overbars and primes denote time averages and perturbations. $e = \frac{1}{2}(\mathbf{u}'^2 + w'^2)$ is the
 381 TKE. The horizontal velocity is decomposed into three components, the Stokes drift component,
 382 \mathbf{u}_s , the geostrophic component, \mathbf{u}_g , and the ageostrophic component, \mathbf{u}_a , each of which has an
 383 associated vertical shear production term. These production terms are denoted LSP, GSP, and
 384 AGSP, respectively. The fourth term on the right-hand side of (1) is the vertical buoyancy
 385 production (VBP) which generates TKE when the ocean surface loses buoyancy through surface
 386 cooling or salt fluxes. The fifth term is the molecular dissipation of TKE. The last term is the
 387 vertical TKE transport. Assuming a steady state and a negligible F_e , an equilibrium is reached
 388 between the TKE dissipation and the TKE sources,

389
$$\epsilon = -\overline{\mathbf{u}'w'} \frac{\partial \overline{u_s}}{\partial z} - \overline{\mathbf{u}'w'} \frac{\partial \overline{u_g}}{\partial z} - \overline{\mathbf{u}'w'} \frac{\partial \overline{u_a}}{\partial z} + \overline{w'b'}. \quad (3)$$

390 This equation can be simplified into a non-dimensional expression for the TKE budget under
 391 destabilizing surface buoyancy forcing at the mid-depth of the OSBL,

392
$$\frac{\epsilon(z=0.5h)}{u_*^3/h} = A_L La_t^{-2} + A_G \frac{h}{L_S} + A_S + A_C La_t^{-2} \frac{h}{L_L}, \quad (4)$$

393 where h is the OSBL thickness as determined by using an offline KPP scheme, $u_* = \sqrt{\frac{|\tau_w|}{\rho}}$ is the
 394 friction velocity (τ_w is the sea surface wind stress, ρ is the seawater density), $La_t = \sqrt{\frac{u_*}{u_s}}$ is the
 395 turbulent Langmuir number⁴⁰. The effect of misalignments between Stokes drift, wind direction
 396 and Langmuir cells is considered in the calculation⁴¹. $L_S = \frac{u_* f}{M^2 \cos \theta}$ is the geostrophic shear stability
 397 length (f is the Coriolis parameter, $M^2 = |\nabla_h b|$ is the horizontal buoyancy gradient magnitude, θ
 398 is the angle between the wind and the frontal geostrophic shear vectors)²⁰, $L_L = \frac{u_*^2 u_s}{B_0}$ is the
 399 Langmuir stability length (B_0 is the sea surface buoyancy flux)¹⁰. Other parameters are taken as
 400 the following values: $A_L = 0.22$, $A_G = 0.5$, $A_S = 2[1 - \exp(-0.5La_t)]$, $A_C = 0.3$. The equation
 401 extends the TKE budget equation of Belcher et al.¹⁰ by including the GSP term. According to
 402 Thomas and Taylor⁴², the GSP production with down-front winds peaks at a value approaching
 403 the Ekman buoyancy flux near the surface and follows a near-linear profile with depth in the
 404 OSBL. So, the parameter $A_G=0.5$ in the GSP term is determined by the vertical structure of GSP
 405 under forced symmetric instability at fronts⁴². In the budget equation, the contribution of
 406 horizontal shear production is not considered, which may become non-negligible at OSBL frontal
 407 regions where the OSBL frontal scale is comparable to the OSBL thickness¹².

408
 409 Here, dynamic processes that lead to dissipation and OSBL deepening are the focus, so
 410 destabilizing sea surface buoyancy flux is considered. Moreover, a steady state of the TKE
 411 budget equation requires an external force for sustained GSP¹⁸, and so only the down-front wind
 412 condition is analyzed⁴². It is noteworthy that this amounts to a conservative estimate of GSP, as it
 413 has been reported elsewhere¹⁶ that VBP tends to interact with GSP and strengthen GSP under
 414 destabilizing conditions and this interaction other transient GSP events are neglected.
 415 Nevertheless, further comparison with the OSMOSIS observations demonstrates the robustness
 416 of the TKE model under surface buoyancy loss which can statistically reproduce OSBL
 417 dissipation (see section below).

418
 419 For each LLC4320 grid point with a wind vector component of down-front winds and destabilizing
 420 sea surface buoyancy flux, the horizontal buoyancy gradient M^2 is calculated and the TKE model
 421 is applied. However, the directly calculated M^2 heavily depends on the spatial resolution. To

422 eliminate this dependence, the calculated M^2 is rescaled according to its spectral characteristic
423 by assuming OSBL fronts are arrested under TTW balance (see sections below). Because OSBL
424 fronts are not always arrested (such as during frontogenesis and frontolysis), the estimation of the
425 submesoscale turbulence here is a maximum magnitude that OSBL fronts can reach, not an
426 average over their whole life. This does not qualitatively alter our results is confirmed above by
427 analysis of the raw model buoyancy gradients, which likewise indicate a leading role for GSP in
428 OSBL turbulence.

429 430 **Validation of the TKE model**

431 To further validate the TKE production model the analysis is applied to in situ observations from
432 the OSMOSIS project^{17, 43} (estimating $\frac{u_*^3}{h}$, La_t , $\frac{h}{L_L}$, and $\frac{h}{L_S}$) and the results are compared to the
433 directly observed dissipation rate. As a part of the OSMOSIS project, nine moorings were
434 deployed in the northeast Atlantic Ocean for the period September 2012–September 2013. With a
435 centrally located mooring, the remaining moorings consisted of two quadrilaterals. It is a
436 13km×13km outer box consisting of four moorings, while it is a 2.5km×2.5km inner one
437 consisting of the remaining four. The resolution of the inner mooring is tended to resolve
438 submesoscale fronts^{17, 43}. The moorings were equipped with Conductivity–Temperature–Depth
439 (CTD) instruments spanning a depth range of 30–530 m with a sampling rate of 5 min. In this
440 work, temperature and salinity observed at the central and inner moorings are used for analysis.
441 Temperature and salinity are interpolated vertically into 10-m bins in the range of 50–300 m. In
442 addition to the mooring array, seagliders were also deployed during the OSMOSIS project, and
443 dissipation rates in the upper ocean were derived from the glider observations⁴⁴.

444
445 In the TKE model, the quantities to be determined are calculated as follows. The OSBL thickness
446 h is determined as the depth where the observed dissipation rate decreases to a threshold value
447 of $1 \times 10^{-8} \text{ W kg}^{-1}$. It should be noted that, from a dynamical perspective, determining the OSBL
448 thickness based on the turbulent dissipation threshold is the most direct and reasonable method.
449 However, since the LLC4320 model uses the KPP turbulence closure scheme, which does not
450 output turbulent dissipation rates but instead determines the OSBL thickness based on the
451 Richardson number—a parameter related to the generation of turbulence due to flow instability—
452 we employed an offline KPP method to determine the OSBL thickness to maintain dynamical
453 consistency with the model results. Then, the dissipation rate at the OSBL mid depth is obtained.
454 The frictional and the convective velocities, u_* and w_* , are calculated based on the atmospheric
455 momentum and buoyancy fluxes provided by the ECMWF ERA5 with a spatial resolution of 0.25°.
456 The Stokes drift u_s , and other wave parameters, are provided from the ECMWF ERA5 with a
457 spatial resolution of 0.5°. The buoyancy gradient M^2 is calculated using the observations of the
458 central and inner moorings. As the inner moorings can only partially resolve submesoscale fronts,
459 we also correct the buoyancy gradient using the rescaling method with the amplification factor
460 derived from the LLC4320.

461
462 The mooring observations are confined below 50 m, hence the validation is conducted in winter
463 (January 2013–April 2013) during which the ocean has a deep OSBL thickness in excess of 100
464 m. All data are interpolated to the times of the glider observations. Furthermore, compared to
465 $C_L = 0.25$, (derived from turbulence resolving numerical simulations), we decide to use $C_L = 1$ in
466 the frontal arrest scale equation which is found to reproduce a better result (**Supplementary Fig.**
467 **8**). As discussed in Bodner et al.²¹, the parameter C_L is on the same order of magnitude as the
468 Richardson number Ri , i.e., $C_L \sim Ri$. In Bodner et al.²¹, shear turbulence is believed to shift Ri to
469 ~ 0.25 based on Large Eddy Simulations (LES). But in the real ocean, the OSBL, especially at
470 frontal regions, tends to stay near a neutral state with $Ri \sim 1$ due to restratification processes¹⁸
471 and geostrophic adjustment^{45, 46} that were not consistently within the scope of the LES setups
472 examined in Bodner et al.²¹, which may explain why using $C_L \sim Ri \sim 1$ tends to reproduce
473 dissipation rates closer to the observations at OSMOSIS. Ri is expected to be regionally dependent

474 over the globe, so using $C_L = 1$ gives a conservative lower bound estimate of the GSP magnitude
475 in this work.

476
477 The expectation is that the produced energy will balance the dissipation of energy, although the
478 transport of energy by the oceanic flow can locally violate this balance. The time series of the
479 dissipation rate at the OSBL mid-depth exhibits dramatic intermittency with variation across
480 several orders of magnitude (**Supplementary Fig. 8a**). When observed dissipation is compared
481 with the summed combination of LSP, VBP and AGSP, the sum is typically too small, especially
482 around the moderate dissipation intensity $\sim 1.0 \times 10^{-7} \text{ W kg}^{-1}$. Including the dissipation from a four-
483 source sum, with GSP, better reproduces the moderate-dissipation events (although it also
484 predicts too few weak dissipation events). PDFs of the dissipation demonstrate the capability of
485 the TKE production model more explicitly (**Supplementary Fig. 8b**). The production without GSP
486 tends to underestimate the observed dissipation—that is a sink stronger than the sources. By
487 contrast, GSP events shift the PDF towards larger values, correcting the underestimation.
488 Notably, the corrected PDF peak is more consistent with observations. With the introduction of
489 GSP the PDF shape has significantly improved, with the results for skewness and kurtosis both
490 indicating a closer match with observations (skewness: from 1.07 to 0.89 compared with 0.9;
491 kurtosis: from 2.75 to 2.19 compared with 2.25).

492
493 A further comparison between the dissipation rates estimated using glider observations and
494 estimates from the LLC4320 simulation is conducted to assess if the buoyancy gradient
495 correction is justified (**Supplementary Fig. 8c**). As there is no overlap between the OSMOSIS
496 winter observation period (January 2013–April 2013) and the winter simulated with LLC4320
497 (here January 2012–April 2012), the non-dimensional values scaled by the simultaneously
498 observed/modeled u_*^3/h are compared. The production from LLC4320 shows a general similarity
499 to the OSMOSIS production, both when GSP is included and excluded—so long as the LLC4320
500 GSP is corrected for limited model resolution (**Supplementary Fig. 8c**). Using only the
501 uncorrected GSP for LLC4320 (i.e., calculated based on the original buoyancy gradients from the
502 LLC4320 without rescaling) underestimates the observed dissipation.

503
504 In addition to the single-point comparison, a comparison over the North Atlantic is also conducted
505 between LLC4320 and eNATL60 to figure out if the result is sensitive to the choice of ocean
506 models. eNATL60 was simulated based on Nucleus for European Modelling of the Ocean
507 (NEMO) covering the North Atlantic with a spatial resolution of $1/60^\circ$. Considering the significant
508 role of GSP turbulence in winter, hourly outputs in Feb 2010 were retrieved. Due to the different
509 simulation periods, the PDFs of the non-dimensional dissipation rates from the four sources are
510 compared (**Supplementary Fig. 9**). The PDF distributions of the four turbulence sources are
511 similar between the two simulations, demonstrating the consistency of the analysis method and
512 results here which are mostly insensitive to the choice among submesoscale-permitting ocean
513 models.

514
515 The result here is quite different from Buckingham et al.⁴³, who reported a less important
516 contribution of GSP to OSBL dissipation. In addition to the buoyancy gradient correction—which
517 adjusts for limitations in the horizontal resolution of the mooring array (**Supplementary Fig. 10**)—
518 another key difference that should be noted is the depth investigated. A fixed depth of 45 m is
519 used in Buckingham et al.⁴³, which is much shallower in winter compared to the mid-depth of the
520 mixed layer used here. LSP turbulence tends to concentrate near the surface and decreases
521 more sharply with depth compared to GSP turbulence. Our work suggests an increasing relative
522 significance of GSP turbulence away from the surface.

523 524 **Buoyancy gradient rescaling**

525 The buoyancy gradient from the LLC4320 is rescaled to account for the effect of horizontal
526 resolution in the numerical model following the method in Fox-Kemper et al.²⁸. The power
527 spectrum of the buoyancy averaged over the OSBL tends to decay with a constant slope (usually

528 around k^{-2}). Thus, the spectrum of the horizontal buoyancy gradient averaged in the OSBL tends
 529 to be flat or white, i.e., $\sim k^0$. Assuming an isotropic, power-law behavior with a spectral slope of k^a
 530 for the buoyancy gradient, the integral of the buoyancy gradient over an integrated domain L_b
 531 range down to the effective model resolution L_{eff} can be related to the wavenumber spectrum
 532 $B_0 k^a$,

$$533 \quad \int_{L_{eff}}^{L_b} \int_0^{2\pi} |\langle \nabla_H b \rangle|^2 r d\theta dr = \int_{\frac{L_{eff}}{L_b}}^{\frac{2\pi}{L_b}} B_0 k^a dk. \quad (5)$$

534 Similarly, the integral from the basin scale down to the frontal scale L_f is

$$535 \quad \int_{L_f}^{L_b} \int_0^{2\pi} |\langle \nabla_H b \rangle|^2 r d\theta dr = \int_{\frac{L_f}{L_b}}^{\frac{2\pi}{L_b}} B_0 k^a dk. \quad (6)$$

536 Combing these two equations yields an estimate for the degree of underestimation of the
 537 modeled buoyancy gradient magnitude relative to that at the frontal scale,

$$538 \quad \frac{\int_{L_{eff}}^{L_b} \int_0^{2\pi} |\nabla_H b|^2 r d\theta dr}{\int_{L_f}^{L_b} \int_0^{2\pi} |\nabla_H b|^2 r d\theta dr} = \frac{\int_{\frac{L_{eff}}{L_b}}^{\frac{2\pi}{L_b}} B_0 k^a dk}{\int_{\frac{L_f}{L_b}}^{\frac{2\pi}{L_b}} B_0 k^a dk} = \left(\frac{L_f}{L_{eff}}\right)^{1+a} \frac{1^{1+a} - \frac{L_{eff}}{L_b}^{1+a}}{1^{1+a} - \frac{L_f}{L_b}^{1+a}} \approx \left(\frac{L_f}{L_{eff}}\right)^{1+a}. \quad (7)$$

539 If $a=0$, the equation scales as estimated in Fox-Kemper et al. ²⁸ ("no-slope corrected"). However,
 540 according to our evaluation based on the LLC4320 result, the spectra in zonal and meridional at
 541 different regions generally have slightly negative slopes, rather than zero slopes (**Supplementary**
 542 **Fig. 11**). Estimates of the slope are therefore derived by linearly fitting over the range determined
 543 by the domain size and the effective resolution $L_{eff} = 7\Delta s$ (this resolution corresponds roughly to
 544 the maximum resolved wavenumber before the spectra roll off sharply due to numerical
 545 dissipation) ³⁴. Based on the slopes over the globe, the original buoyancy gradient magnitude
 546 derived directly from LLC4320 ("uncorrected") is rescaled based on the estimated true frontal
 547 width ("corrected") by,

$$548 \quad \nabla_H b_f = \left(\frac{L_{eff}}{L_f}\right)^{\frac{1+a}{2}} \nabla_H b_{\Delta s}. \quad (8)$$

549 It should be noted that the amplification factor $\left(\frac{L_{eff}}{L_f}\right)^{\frac{1+a}{2}}$ is directly taken as 1 at low latitudes when
 550 $L_{eff} < L_f$, i.e., where fronts are resolved. As shown in **Supplementary Fig. 12**, the amplification
 551 factor $\left(\frac{L_{eff}}{L_f}\right)^{\frac{1+a}{2}}$ exceeds 6 at mid-latitudes. The correction dynamically reproduces the buoyancy
 552 gradient associated with small-scale submesoscale fronts that are not resolved by the LLC4320
 553 simulation.

555 Calculation of frontal arrest scale

556 Geostrophic adjustment theory predicts that the width of a front tends to follow the local
 557 deformation radius ⁴⁶. But in the OSBL, strong turbulence breaks the geostrophic balance, and
 558 near-surface fronts are sharpened by strain-induced and surface-induced frontogenesis until they
 559 are arrested at a smaller scale by surface-forced turbulence, typically on a scale where TTW
 560 balance holds ^{12, 47, 48, 49}. Thus, the front width under TTW is believed to be the scale where the
 561 fronts in the OSBL are arrested and persistent. For the TTW balance,

$$562 \quad \nabla_H b = -f \mathbf{k} \times \frac{\partial \bar{\mathbf{u}}}{\partial z} + \frac{\partial^2}{\partial z^2} (\mathbf{u}' w'), \quad (9)$$

563 the Reynolds stress term can be parameterized as $\mathbf{u}' w' = (m_* u_*^3 + n_* w_*^3)^{2/3}$ from the planetary
 564 boundary layer scheme (ePBL; Reichl and Hallberg, 2018). Thus, a scaling method for the
 565 arrested frontal width is proposed by Bodner et al. ²¹,

$$566 \quad L_f = C_L \frac{(m_* u_*^3 + n_* w_*^3)^{2/3}}{f^2 h}. \quad (10)$$

567 Here, only destabilizing surface buoyancy forcing that produces TKE is considered. Under the
568 destabilizing condition, the mechanical coefficient m_* measures the efficiency of the mechanical
569 forcing in changing OSBL TKE and is scaled by combining Equations (29) and (36) of Reichl and
570 Hallberg⁵⁰ rather than a constant as in Bodner et al.²¹, while the convection coefficient $n_* = 0.066$
571 measures the efficiency of the buoyancy forcing in changing OSBL TKE and is taken as a
572 constant. $w_* = (B_0 h)^{1/3}$ is the convective velocity. f is the Coriolis parameter, h is the OSBL
573 thickness, and C_L is a constant parameter. In this work, we decide to use a more conservative
574 value of $C_L = 1$ based on a comparison with observations (Text S1) instead of $C_L = 0.25$
575 suggested by Bodner et al.²¹ based on a limited number of LES. Details are referred to Bodner et
576 al.²¹. Till now, no direct observations of arrested OSBL fronts have been reported globally.
577 However, as discussed in Bodner et al.²¹ and also compared with indirect observations⁵¹ and
578 other LES results¹², the theory reproduces dynamically consistent frontal scale. The arrest scale
579 here provides a dynamically lower bound of the frontal width for the buoyancy gradient rescaling,
580 since not every OSBL front reaches its arrest scale in the real ocean.

581

582 The frontal width is calculated based on the LLC4320 outputs. We evaluate the robustness of that
583 dataset using a simulation of upper ocean mixing without feedback using the General Ocean
584 Turbulence Model (GOTM). GOTM is a one-dimensional water column model that is focused on
585 ocean turbulence⁵². The version of GOTM used here is compiled with the ePBL closure^{11,50}. On
586 each grid point of the subsampled 4^o LLC4320 grids, GOTM simulation is conducted for two
587 months, February and August. The initial and boundary conditions are provided by LLC4320. For
588 consistency, we also directly use the outputted sea surface fluxes from the simulation, which are
589 provided by the ECMWF dataset. The vertical spacings of the simulations are as fine as
590 centimeters, which ensures the capability of the GOTM in reproducing the OSBL. As Bodner et al.
591²¹ proposed the frontal arrest scale based on the ePBL, we apply the ePBL scheme in the GOTM
592 simulations. Hence, the frontal scale calculated from the GOTM outputs tends to be more
593 dynamically consistent.

594

595 By comparing the frontal scales between the GOTM and LLC4320, we can estimate the
596 sensitivity of the frontal width to the sub-grid turbulence closures (**Supplementary Fig. 13**). The
597 frontal width over the globe varies across several orders of magnitude with latitude, from
598 hundreds of meters to tens of kilometers. The frontal width is larger in summer than in winter.
599 Despite using different sub-grid turbulence schemes (KPP in LLC4320 and ePBL in GOTM), the
600 calculated frontal widths resemble each other which demonstrates that the frontal scale
601 calculated here is insensitive to the turbulence closures. Finally, while the GSP and horizontal
602 shear production of the fronts themselves should contribute somewhat to the turbulence causing
603 the arrest, the robustness of the frontal width estimates to various TKE energy sources indicates
604 these effects are unlikely to change the result significantly. These results indicates that the
605 calculated frontal width is not sensitive to the details of the model and its chosen sub-grid
606 turbulence closure.

607

608 **Data availability**

609 The LLC4320 data can be directly accessed from the ECCO Data Portal
610 (<https://data.nas.nasa.gov/ecco/data.php>), or conveniently downloaded using the xmitgcm
611 package (<https://xmitgcm.readthedocs.io/en/latest/index.html>). The Stokes drift of the ECMWF
612 ERA5 is accessible at the Copernicus Climate Change Service (C3S) Climate Data Store
613 (<https://cds.climate.copernicus.eu/cdsapp#!/dataset/reanalysis-era5-single-levels?tab=form>). The
614 OSMOSIS data is available at the British Oceanographic Data Centre after registration
615 (https://www.bodc.ac.uk/data/bodc_database/nodb/search/). The VIIRS L2 SST product is
616 available at the JPL Physical Oceanography Distributed Active Archive Center
617 (<https://doi.org/10.5067/GHVRS-2PO28>). Source data are provided with this paper.

618

619 **Code availability**

620 The codes used for generating the figures in the paper can be accessed at

621 <https://doi.org/10.5281/zenodo.13954663>.
622
623
624
625

626 **References**

- 627 1. Fox-Kemper B, Johnson L, Qiao F. Chapter 4 - Ocean near-surface layers. In: Meredith M,
628 Naveira Garabato A (eds). *Ocean Mixing*. Elsevier, 2022, pp 65-94.
629
- 630 2. McCartney MS. Subantarctic mode water. *Woods Hole Oceanographic Institution*
631 *Contribution* 1979, **3773**: 103-119.
632
- 633 3. Sallée JB, Shuckburgh E, Bruneau N, Meijers AJ, Bracegirdle TJ, Wang Z. Assessment of
634 Southern Ocean mixed - layer depths in CMIP5 models: Historical bias and forcing
635 response. *Journal of Geophysical Research: Oceans* 2013, **118**(4): 1845-1862.
636
- 637 4. Thomas MD, Tréguier A-M, Blanke B, Deshayes J, Voltaire A. A Lagrangian method to
638 isolate the impacts of mixed layer subduction on the meridional overturning circulation in
639 a numerical model. *Journal of Climate* 2015, **28**(19): 7503-7517.
640
- 641 5. Frankignoul C, Hasselmann K. Stochastic climate models, Part II Application to sea-surface
642 temperature anomalies and thermocline variability. *Tellus* 1977, **29**(4): 289-305.
643
- 644 6. Price JF, Weller RA, Pinkel R. Diurnal cycling: Observations and models of the upper ocean
645 response to diurnal heating, cooling, and wind mixing. *Journal of Geophysical Research:*
646 *Oceans* 1986, **91**(C7): 8411-8427.
647
- 648 7. Klein P, Coste B. Effects of wind-stress variability on nutrient transport into the mixed layer.
649 *Deep Sea Research Part A Oceanographic Research Papers* 1984, **31**(1): 21-37.
650
- 651 8. Rodgers KB, Aumont O, Mikaloff Fletcher S, Plancherel Y, Bopp L, de Boyer Montégut C, *et*
652 *al.* Strong sensitivity of Southern Ocean carbon uptake and nutrient cycling to wind stirring.
653 *Biogeosciences* 2014, **11**(15): 4077-4098.
654
- 655 9. Large WG, McWilliams JC, Doney SC. Oceanic vertical mixing: A review and a model with
656 a nonlocal boundary layer parameterization. *Reviews of geophysics* 1994, **32**(4): 363-403.
657
- 658 10. Belcher SE, Grant AL, Hanley KE, Fox - Kemper B, Van Roekel L, Sullivan PP, *et al.* A global
659 perspective on Langmuir turbulence in the ocean surface boundary layer. *Geophysical*
660 *Research Letters* 2012, **39**(18).
661
- 662 11. Li Q, Reichl BG, Fox - Kemper B, Adcroft AJ, Belcher SE, Danabasoglu G, *et al.* Comparing
663 ocean surface boundary vertical mixing schemes including Langmuir turbulence. *Journal*
664 *of Advances in Modeling Earth Systems* 2019, **11**(11): 3545-3592.
665
- 666 12. Sullivan PP, McWilliams JC. Frontogenesis and frontal arrest of a dense filament in the
667 oceanic surface boundary layer. *Journal of Fluid Mechanics* 2018, **837**: 341-380.
668
- 669 13. Zheng Z, Harcourt RR, D'Asaro EA. Evaluating Monin–Obukhov Scaling in the Unstable
670 Oceanic Surface Layer. *Journal of Physical Oceanography* 2021, **51**(3): 911-930.

- 671
672 14. Ferris L, Gong D, Clayson CA, Merrifield S, Shroyer EL, Smith M, *et al.* Shear turbulence in
673 the high-wind Southern Ocean using direct measurements. *Journal of Physical*
674 *Oceanography* 2022, **52**(10): 2325-2341.
675
676 15. D'asaro E, Lee C, Rainville L, Harcourt R, Thomas L. Enhanced turbulence and energy
677 dissipation at ocean fronts. *science* 2011, **332**(6027): 318-322.
678
679 16. Thomas LN, Taylor JR, Ferrari R, Joyce TM. Symmetric instability in the Gulf Stream. *Deep*
680 *Sea Research Part II: Topical Studies in Oceanography* 2013, **91**: 96-110.
681
682 17. Yu X, Naveira Garabato AC, Martin AP, Gwyn Evans D, Su Z. Wind - forced symmetric
683 instability at a transient mid - ocean front. *Geophysical Research Letters* 2019, **46**(20):
684 11281-11291.
685
686 18. Bachman SD, Fox-Kemper B, Taylor JR, Thomas LN. Parameterization of frontal symmetric
687 instabilities. I: Theory for resolved fronts. *Ocean Modelling* 2017, **109**: 72-95.
688
689 19. Wenegrat JO, Thomas LN, Sundermeyer MA, Taylor JR, D'Asaro EA, Klymak JM, *et al.*
690 Enhanced mixing across the gyre boundary at the Gulf Stream front. *Proceedings of the*
691 *National Academy of Sciences* 2020, **117**(30): 17607-17614.
692
693 20. Skillingstad ED, Duncombe J, Samelson RM. Baroclinic frontal instabilities and turbulent
694 mixing in the surface boundary layer. Part II: Forced simulations. *Journal of Physical*
695 *Oceanography* 2017, **47**(10): 2429-2454.
696
697 21. Bodner AS, Fox-Kemper B, Johnson L, Van Roekel LP, McWilliams JC, Sullivan PP, *et al.*
698 Modifying the Mixed Layer Eddy Parameterization to Include Frontogenesis Arrest by
699 Boundary Layer Turbulence. *Journal of Physical Oceanography* 2022.
700
701 22. Su Z, Wang J, Klein P, Thompson AF, Menemenlis D. Ocean submesoscales as a key
702 component of the global heat budget. *Nature communications* 2018, **9**(1): 1-8.
703
704 23. Cael BB, Mashayek A. Log-Skew-Normality of Ocean Turbulence. *Physical Review Letters*
705 2021, **126**(22): 224502.
706
707 24. Pearson B, Fox-Kemper B. Log-normal turbulence dissipation in global ocean models.
708 *Physical review letters* 2018, **120**(9): 094501.
709
710 25. Dong J, Fox - Kemper B, Zhang H, Dong C. The seasonality of submesoscale energy
711 production, content, and cascade. *Geophysical Research Letters* 2020, **47**(6):
712 e2020GL087388.
713
714 26. Callies J, Ferrari R, Klymak JM, Gula J. Seasonality in submesoscale turbulence. *Nature*
715 *Communications* 2015, **6**(1): 6862.
716

- 717 27. Dong J, Fox-Kemper B, Zhang H, Dong C. The scale of submesoscale baroclinic instability
718 globally. *Journal of Physical Oceanography* 2020, **50**(9): 2649-2667.
719
- 720 28. Fox-Kemper B, Danabasoglu G, Ferrari R, Griffies S, Hallberg R, Holland M, *et al.*
721 Parameterization of mixed layer eddies. III: Implementation and impact in global ocean
722 climate simulations. *Ocean Modelling* 2011, **39**(1-2): 61-78.
723
- 724 29. Moeng C-H, Sullivan PP. A comparison of shear-and buoyancy-driven planetary boundary
725 layer flows. *Journal of Atmospheric Sciences* 1994, **51**(7): 999-1022.
726
- 727 30. Mahadevan A, D'asaro E, Lee C, Perry MJ. Eddy-driven stratification initiates North Atlantic
728 spring phytoplankton blooms. *Science* 2012, **337**(6090): 54-58.
729
- 730 31. Taylor JR. Turbulent mixing, restratification, and phytoplankton growth at a submesoscale
731 eddy. *Geophysical Research Letters* 2016, **43**(11): 5784-5792.
732
- 733 32. Eden C, Czeschel L, Olbers D. Toward Energetically Consistent Ocean Models. *Journal of*
734 *Physical Oceanography* 2014, **44**(12): 3160-3184.
735
- 736 33. Menemenlis D, Campin J-M, Heimbach P, Hill C, Lee T, Nguyen A, *et al.* ECCO2: High
737 resolution global ocean and sea ice data synthesis. *Mercator Ocean Quarterly Newsletter*
738 2008, **31**(October): 13-21.
739
- 740 34. Rocha CB, Chereskin TK, Gille ST, Menemenlis D. Mesoscale to submesoscale wavenumber
741 spectra in Drake Passage. *Journal of Physical Oceanography* 2016, **46**(2): 601-620.
742
- 743 35. Rocha CB, Gille ST, Chereskin TK, Menemenlis D. Seasonality of submesoscale dynamics in
744 the Kuroshio Extension. *Geophysical Research Letters* 2016, **43**(21): 11,304-311,311.
745
- 746 36. Viglione GA, Thompson AF, Flexas MM, Sprintall J, Swart S. Abrupt transitions in
747 submesoscale structure in Southern Drake Passage: Glider observations and model results.
748 *Journal of Physical Oceanography* 2018, **48**(9): 2011-2027.
749
- 750 37. Gallmeier KM, Prochaska JX, Cornillon P, Menemenlis D, Kelm M. An evaluation of the
751 LLC4320 global ocean simulation based on the submesoscale structure of modeled sea
752 surface temperature fields. *Geoscientific Model Development Discussions* 2023: 1-42.
753
- 754 38. Yu K, Dong C, King GP. Turbulent kinetic energy of the ocean winds over the Kuroshio E
755 xtension from Quik SCAT winds (1999–2009). *Journal of Geophysical Research: Oceans*
756 2017, **122**(6): 4482-4499.
757
- 758 39. Dong J, Fox-Kemper B, Zhang H, Dong C. The Scale and Activity of Symmetric Instability
759 Estimated from a Global Submesoscale-Permitting Ocean Model. *Journal of Physical*
760 *Oceanography* 2021, **51**(5): 1655-1670.
761
- 762 40. McWILLIAMS JC, Sullivan PP, Moeng C-H. Langmuir turbulence in the ocean. *Journal of*

763 *Fluid Mechanics* 1997, **334**: 1-30.
764

765 41. Van Roekel L, Fox - Kemper B, Sullivan P, Hamlington P, Haney S. The form and orientation
766 of Langmuir cells for misaligned winds and waves. *Journal of Geophysical Research:*
767 *Oceans* 2012, **117**(C5).
768

769 42. Thomas LN, Taylor JR. Reduction of the usable wind - work on the general circulation by
770 forced symmetric instability. *Geophysical Research Letters* 2010, **37**(18).
771

772 43. Buckingham CE, Lucas NS, Belcher SE, Rippeth TP, Grant AL, Le Sommer J, *et al.* The
773 contribution of surface and submesoscale processes to turbulence in the open ocean
774 surface boundary layer. *Journal of Advances in Modeling Earth Systems* 2019, **11**(12):
775 4066-4094.
776

777 44. Evans DG, Lucas NS, Hemsley V, Frajka - Williams E, Naveira Garabato AC, Martin A, *et al.*
778 Annual cycle of turbulent dissipation estimated from Seaglidrs. *Geophysical Research*
779 *Letters* 2018, **45**(19): 10,560-510,569.
780

781 45. Tandon A, Garrett C. Geostrophic adjustment and restratification of a mixed layer with
782 horizontal gradients above a stratified layer. *Journal of physical oceanography* 1995,
783 **25**(10): 2229-2241.
784

785 46. Tandon A, Garrett C. Mixed layer restratification due to a horizontal density gradient.
786 *Journal of Physical Oceanography* 1994, **24**(6): 1419-1424.
787

788 47. Gula J, Molemaker MJ, McWilliams JC. Submesoscale cold filaments in the Gulf Stream.
789 *Journal of Physical Oceanography* 2014, **44**(10): 2617-2643.
790

791 48. McWilliams JC, Gula J, Molemaker MJ, Renault L, Shchepetkin AF. Filament frontogenesis
792 by boundary layer turbulence. *Journal of Physical Oceanography* 2015, **45**(8): 1988-2005.
793

794 49. Wenegrat JO, McPhaden MJ. Wind, waves, and fronts: Frictional effects in a generalized
795 Ekman model. *Journal of Physical Oceanography* 2016, **46**(2): 371-394.
796

797 50. Reichl BG, Hallberg R. A simplified energetics based planetary boundary layer (ePBL)
798 approach for ocean climate simulations. *Ocean Modelling* 2018, **132**: 112-129.
799

800 51. Ramachandran S, Tandon A, Mackinnon J, Lucas AJ, Pinkel R, Waterhouse AF, *et al.*
801 Submesoscale processes at shallow salinity fronts in the Bay of Bengal: Observations
802 during the winter monsoon. *Journal of Physical Oceanography* 2018, **48**(3): 479-509.
803

804 52. Lars Umlauf HBaKB. GOTM: Source code and Test Case Documentation Version 4.0; 2005.
805
806

807

808 **Acknowledgments**

809 The authors wish to thank the Estimating the Circulation and Climate of the Oceans (ECCO) team
810 (<https://ecco.jpl.nasa.gov>) and NASA High-End Computing (HEC) from the NASA Advanced
811 Superconducting (NAS) Division at the Ames Research Center for the LLC4320 simulation data.

812 The authors also thank Hong Zhang's help for downloading the LLC4320 data, and Aurélie Albert
813 for sharing the eNATL60 data. This work is supported by the National Natural Science
814 Foundation of China (42176023, 42192562, 42361144844, 42206002). J.W. was supported by
815 the National Science Foundation under grant OCE-2148945. B.F-K. was supported by NSF OCE-
816 2148945 and NOAA NA19OAR4310366.

817

818

819 **Author contributions**

820 J.D., B.F. and J.W. conceived the experiments, analyzed the results and wrote the manuscript.

821 A.B. helped with the analysis of the numerical simulations. Y.X. helped with the analysis of the

822 observations. J.D., B.F., J.W., A.B., S.B. and C.D. reviewed the manuscript.

823

824 **Competing interests**

825 The authors declare no competing interests.

826

827 **Additional information**

828 Supplementary information is available for this paper at .

829

830 **Figure captions**

831

832 **Fig. 1 Three-dimensional global probability density of the three parameters.** **a**, The
833 probability density in winter. **b**, The probability density in summer. The three parameters are
834 turbulent Langmuir number La_t of the x-axis, the ratio of the boundary layer depth to the Langmuir
835 stability length h/L_L of the y-axis, and the ratio of the boundary layer depth to the geostrophic
836 shear stability length h/L_s of the z-axis. Two-dimensional projections of the distributions are also
837 shown. The black contours enclose 30%, 60%, and 90% of the global values. Each source of
838 turbulence is labeled (GSP: geostrophic shear production turbulence; LSP: Langmuir shear
839 production turbulence; VBP: vertical buoyancy production turbulence; AGSP: ageostrophic shear
840 production turbulence) and the contribution of fronts (i.e., GSP) is highlighted as the geostrophic
841 shear along the z-axis is increased. Source data are provided as a Source Data file.

842

843 **Fig. 2 Turbulence regimes in parameter slices in winter.** **a**, $h/L_s=0.1$. **b**, $h/L_s=5$. **c**, $h/L_s=50$. **d**,
844 $h/L_L=0.1$. **e**, $h/L_L=1$. **f**, $h/L_L=10$. **g**, $La_t=0.1$. **h**, $La_t=0.3$. **i**, $La_t=0.8$. The regimes (GSP: geostrophic
845 shear production turbulence; LSP: Langmuir shear production turbulence; VBP: vertical buoyancy
846 production turbulence; AGSP: ageostrophic shear production turbulence) denoted by different
847 color patches are defined by the dominant production terms in the turbulent kinetic energy (TKE)
848 budget. The white contours enclose 30%, 60%, and 90% of the locations with the corresponding
849 values. A regime is considered dominant when its contribution exceeds 75% of the total
850 dissipation, otherwise, it is a two-turbulence-mixed regime when two TKE sources both contribute
851 more than 25% while all others contribute less than 25%, and lastly, it is a mixed regime if more
852 than three sources of turbulence contribute more than 25% ¹¹. The distributions indicate that GSP
853 is an important regime for ocean surface boundary layer turbulence over the globe, especially at
854 locations with strong frontal geostrophic shears. Source data are provided as a Source Data file.

855

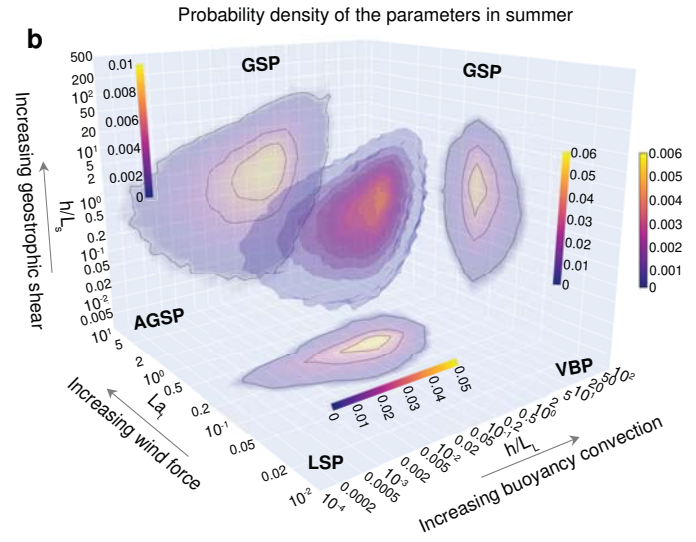
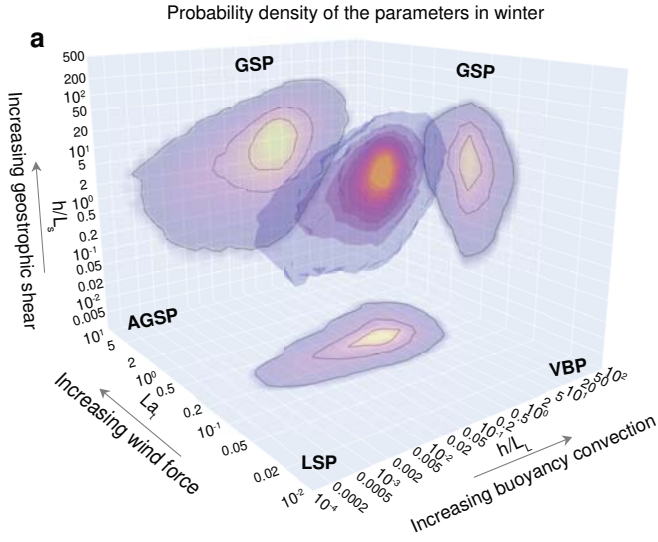
856 **Fig. 3 Probability density functions (PDFs) of the turbulence sources.** **a**, PDFs of the four
857 sources, geostrophic shear production turbulence, (GSP; orange), Langmuir shear production
858 turbulence (LSP; dark blue), vertical buoyancy production turbulence (VBP; light blue),
859 ageostrophic shear production turbulence (AGSP; dark red). in winter. **b**, PDFs of the four
860 sources in summer. The dots indicate the corresponding global mean value of each distribution.
861 The log-normal distribution of the PDFs suggests that the mean and integral of ocean surface
862 boundary layer dissipation are determined by intermittent high dissipation rates. The highest
863 intermittency of GSP can also be derived from the distributions. Source data are provided as a
864 Source Data file.

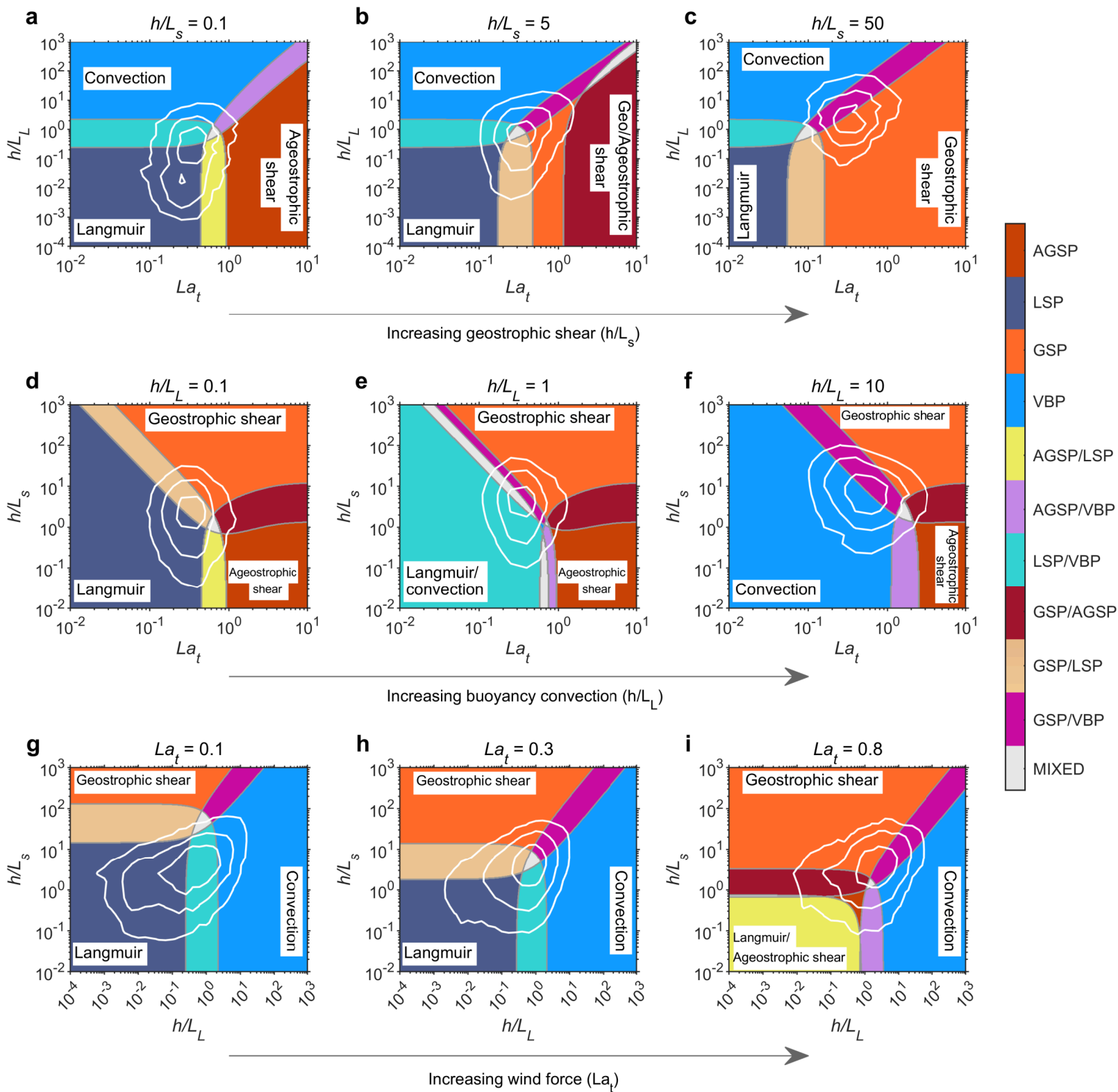
865

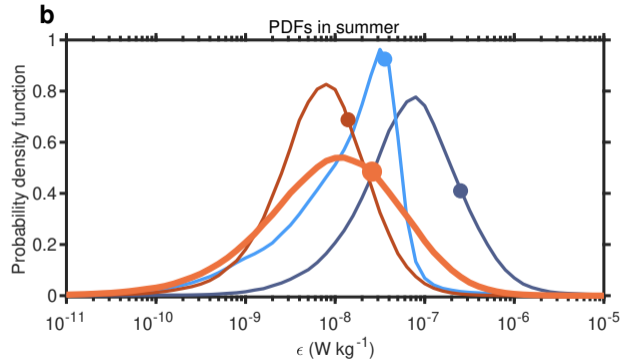
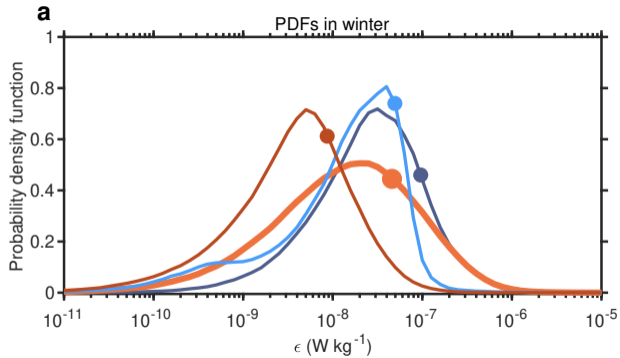
866 **Fig. 4 Global distributions of the two most likely dominant sources at each location.** **a**, The
867 first most likely dominant sources (GSP: geostrophic shear production turbulence; LSP: Langmuir
868 shear production turbulence; VBP: vertical buoyancy production turbulence; AGSP: ageostrophic
869 shear production turbulence) in winter. **b**, The second most likely dominant sources in winter. **c**,
870 The first most likely dominant sources in summer. **d**, The second most likely dominant sources in
871 summer. Their relative contribution percentages to the total mean dissipation (%) are shown in **e**-
872 **h**. The relative contributions shown in **e-h** indicate that the summation of the top two sources can
873 explain most ($Pct_{1st} + Pct_{2nd} > 55\%$) of the total dissipation. GSP turbulence is the first largest
874 contributor at low and mid latitudes in winter, and still the second largest contributor at high
875 latitudes in both seasons. Source data are provided as a Source Data file.

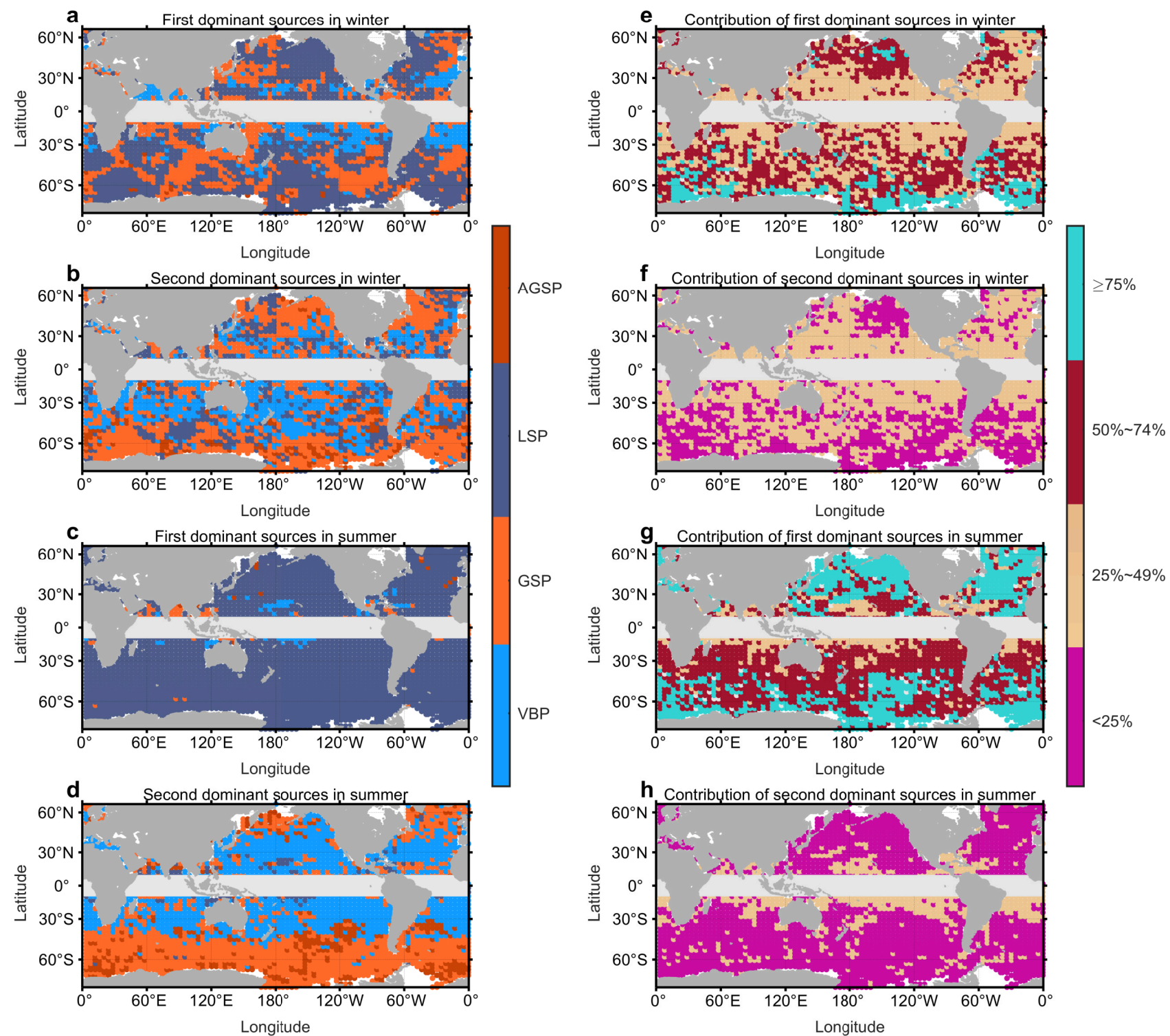
876 **Fig. 5 A schematic diagram of the four turbulence sources.** Geostrophic shear production
877 turbulence (GSP), Langmuir shear production turbulence (LSP), vertical buoyancy production
878 turbulence (VBP), and ageostrophic shear production turbulence (AGSP) represent the
879 turbulence sources from Langmuir circulation, geostrophic current shear, vertical convection, and

880 ageostrophic current shear. LSP is the shear to turbulence from Stokes drifts due to winds and
881 waves. GSP is the shear to turbulence from geostrophic currents at fronts with down-front winds.
882 VBP is the convection to turbulence by gravitational instability due to surface buoyancy loss.
883 AGSP is the shear to turbulence from ageostrophic currents induced by winds. The left two pie
884 charts show the spatial prevalence of each turbulence source in winter and summer, while the
885 right two show the relative contribution of each source to the total dissipation magnitude averaged
886 over the globe (LSP: dark blue; GSP: orange; VBP: light blue; AGSP: dark red). These
887 percentages indicate that GSP is a prevalent and significant source of OSBL turbulence over the
888 globe. Source data are provided as a Source Data file.
889
890









Four turbulence sources and their prevalence and contributions

